Investigation of High Oxygen Reduction Reaction Catalytic Performance on Mn-Based Mullite $SmMn_2O_5$

UT Dallas Author(s):

Weichao Wang

Citation:

Liu, Jieyu, Meng Yu, Xuewei Wang, Jie Wu, et al. 2017. "Investigation of high oxygen reduction reaction catalytic performance on Mn-based mullite SmMn2O5." Journal of Materials Chemistry A 5(39): 20922-20931.

Journal of Materials Chemistry A

PAPER

View Article Online
View Journal | View Issue

Cite this: J. Mater. Chem. A, 2017, 5, 20922

Investigation of high oxygen reduction reaction catalytic performance on Mn-based mullite $SmMn_2O_5$†

Jieyu Liu, ‡[a] Meng Yu,‡[a] Xuewei Wang,[b] Jie Wu,[c] Changhong Wang,[d] Lijun Zheng,[a] Dachi Yang, [a] Hui Liu,[a] Yan Yao, [e] Feng Lu*[a] and Weichao Wang *[af]

Received 4th April 2017
Accepted 5th September 2017

DOI: 10.1039/c7ta02905e

rsc.li/materials-a

An alternative material $SmMn_2O_5$ mullite with regard to Pt/C is proposed to catalyze the oxygen reduction reaction (ORR) by combining density functional theory (DFT) calculations and experimental validations. Theoretical calculations are performed to investigate the bulk phase diagram, as well as the stability and electrocatalytic activity of the ORR under alkaline conditions for $SmMn_2O_5$ (001) surfaces, which are passivated by nitrogen atoms to avoid any spurious interference. The adsorptions of relevant ORR species (O*, OH*, OOH* and OO*) tend to compensate the coordination of manganese atoms to form Mn-centered octahedral or pyramidal crystal fields, and the corresponding binding energies fulfill a linear relationship. An oxygen molecule prefers to be reduced to OH^- *via* a four-electron pathway and this prediction is verified by electrochemical measurements on the as-prepared $SmMn_2O_5$ catalyst with a nanorod structure. Volcano curves are obtained to describe the trends in theoretical ORR activity as a function of a single parameter, *i.e.* the oxygen binding energy. An overpotential of 0.43 V is obtained at the O* binding energy around 3.4 eV, which is close to the experimental observation (0.413 V) in this work. $SmMn_2O_5$ mullite exhibits favorable ORR activity and superior stability with only ~5% decay in activity over 20 000 s of chronoamperometric operation in contrast to ~15% decrease of Pt/C, making it a promising candidate for a cathode catalyst.

Introduction

Searching earth-abundant and cost-effective materials to replace precious platinum-based electrocatalysts for boosting the oxygen reduction reaction (ORR) activity at the cathode of fuel cells is of primary significance in developing renewable energy storage and conversion devices. A considerable amount of exploration has been undertaken in search of substitutes to meet the demands of large-scale commercialization of electrocatalysts. Transition metal oxides (TMOs) have attracted great attention since the d-orbitals of the active transition metal cations are flexible to exchange electrons with external species, which is the fundamental origin of the catalytic activity of TMOs.[1] Cobalt oxides and manganese oxides are the most studied TMOs for ORR catalysis. Extensive efforts have been devoted to improving their activities by optimizing the morphology, surface area and active sites.[2–6] In recent decades, the properties of ternary oxides with the AB_mO_n structure, where A denotes a rare-earth or alkaline earth cation and B a transition metal cation, have been widely explored, resulting from a tunable electronic structure and further enhanced stability.[7] The perovskite-type oxides (ABO_3) are promising candidate materials due to the flexibility of tuning the A or B element and thus optimizing their ORR catalytic activities.[8] Significant progress has been achieved to explain the fundamentals of the ORR mechanism, such as the metal's d-band center relative to its Fermi level.[9] Yang *et al.* proposed that the σ*-antibonding (e_g) orbital occupation and B-site transition-metal-oxygen covalence govern the ORR activity on perovskite oxide catalysts.[8]

Importantly, these TMOs also demonstrate superior catalytic activities in NO oxidation. Cobalt-based catalysts supported on titania and zirconia are effective for the oxidation of nitric oxide to nitrogen dioxide.[10] Manganese oxide catalysts precipitated with sodium carbonate and calcined in air at moderate temperatures show high activities for low temperature selective

[a]College of Electronic Information and Optical Engineering, Nankai University, Tianjin 300350, China. E-mail: weichaowang@nankai.edu.cn; lufeng@nankai.edu.cn
[b]School of Materials Science and Engineering, Tianjin University of Technology, Tianjin 300384, China
[c]College of Material Science and Engineering, Shandong University of Science and Technology, Qingdao 266590, China
[d]School of Science, Tianjin University of Technology, Tianjin 300384, China
[e]Department of Electrical and Computer Engineering, Materials Science and Engineering Program, University of Houston, Houston, TX 77204, USA
[f]Department of Materials Science and Engineering, University of Texas at Dallas, Richardson, TX 75080, USA

† Electronic supplementary information (ESI) available: Computational details for the bulk $SmMn_2O_5$ mullite phase diagram, the stability of mullite $SmMn_2O_5$ (001) surfaces, the linear relationship of binding energies for ORR intermediates, the theoretical activity and the two-electron pathway; the synthesis method of the pure-phase $SmMn_2O_5$; electrode preparation and the process of the electrochemical analysis. See DOI: 10.1039/c7ta02905e

‡ These authors contributed equally to this work.

catalytic reduction of NO_x with NH_3.[11] The lanthanum-based perovskite catalysts doped with strontium have been reported to achieve a high NO-to-NO_2 conversion rate under realistic conditions.[12]

There are still open questions why the ORR and NO oxidation share the same catalysts. Probably, the moderate p–d hybridization strength during chemical reactions plays an important role in governing the catalytic process.[13,14] Inspired by this idea, we note one new class of Mn-based mullites (with $SmMn_2O_5$ as a typical representative) which exhibit superior catalytic activities for NO oxidation with regard to platinum-based commercial catalysts.[15] There are two different Mn coordinations (octahedral Mn^{4+} and pyramidal Mn^{3+}) in $SmMn_2O_5$, making the local surface structures plentiful and facilitating the tunability of the electronic structure. The active sites have been identified in the Mn–Mn dimers which display Mn^{4+}, *i.e.* partial d-orbital filling.[15] We thus expect that this group of materials could be applied to the ORR as well. In our previous work, we have reported that the mixed-phase mullite exhibits comparable ORR catalytic activity and superior stability to Pt/C.[16] $SmMn_2O_5$ is supposed to be ORR-active in the mixed-phase mullite. Density functional theory (DFT) simulations show that the moderate bond strength between adsorbed O atoms and pyramidal Mn dimmer sites is essential for ORR catalytic activity.[16] However, the origin of the electrochemical activity of pure-phase mullite $SmMn_2O_5$ is still unclear and the processes occurring at its surfaces have not yet been systematically studied, especially on the atomic and molecular scales, which is of great significance to optimize the current mullite-based ORR catalysts and further design new effective non-precious metal catalysts.

In this work, we investigate the properties of the bulk, ideal and stepped surfaces of $SmMn_2O_5$ along the (001) direction through DFT calculations. In order to clarify the reaction mechanisms, we study adsorptions of ORR intermediates (O*, OH*, OOH* and OO*) on $SmMn_2O_5$ (001) surfaces with different atomic terminations. The scaling relationships of binding energies of O*, OH*, OOH* and OO* are presented. The theoretical activity of the charge transfer steps is depicted as a function of the oxygen binding energy, which produces volcano curves to describe trends in ORR activity. $SmMn_2O_5$ mullite with a nanorod structure is successfully synthesized through a hydrothermal method and our experimentally observed overpotential is 0.413 V, being consistent with the calculated value (~0.43 V). This mullite-based catalyst exhibits a similar limiting current density and superior stability to a commercial Pt/C catalyst. This work displays that $SmMn_2O_5$ mullite could be a promising alternative catalyst to replace Pt/C, and also, provides insights into the rational design of oxide catalysts.

Computational and experimental methods

Ab initio calculations were carried out based on the DFT method. The generalized gradient approximation (GGA) exchange–correlation with the PW91 version and a plane wave basis, as implemented in the VASP code, were employed.[17–19] Electron-ion interactions were treated by the projector augmented wave (PAW) method.[20] The plane wave cutoff was 400 eV. All calculations were spin polarized. The convergence criterion for energy was 10^{-4} eV between two electronic steps. In the bulk calculations, a Γ-centered k-mesh of $(3 \times 5 \times 8)$ was used. Both lattice constants and atomic positions were optimized until the maximum force on each atom was less than 0.01 eV $Å^{-1}$.

In the surface calculations, the $p(2 \times 1)$ supercell with a Γ-centered k-mesh of $(2 \times 4 \times 1)$ was applied. To avoid interactions between images in the periodic slab model, a vacuum with a thickness of 15 Å was adopted. Bottom pseudo-surface atoms were passivated by N atoms to avoid the spurious interference between top and bottom surfaces. Both N and bottom Sm–O atomic layers were kept fixed, while the remaining slab coordinates and the adsorbates were internally relaxed. Geometry optimization of the (001) slab coordinates was first performed without adsorbates until the force on each unconstrained atom was below 0.01 eV $Å^{-1}$. The oxygen-containing species (O*, OH*, OO*, and OOH*) were then adsorbed on the surfaces using a force threshold of 0.05 eV $Å^{-1}$.

A pure-phase mullite $SmMn_2O_5$ catalyst sample was prepared following a hydrothermal method based on previous research with minor modification.[21] Briefly, samarium nitrate and manganese acetate at the respective stoichiometric ratio were dissolved in deionized water. After being titrated with an appropriate amount of sodium hydroxide solution, the mixture was transferred into an autoclave and treated at 200 °C for 24 h. Details can be found in Section S7 in the ESI.† The phase characterization of the catalyst sample was conducted by X-ray diffraction (Ultima IV, Rigaku Corp.). The radiation source was Cu Kα (λ = 0.1542 Å) operating at 40 kV and 40 mA at 8° min^{-1} with an interval of 0.02°. Scanning electron microscopy (SEM) images were recorded with a ZEISS 6164 scanning electron microanalyzer operating at 5 kV. Transmission electron microscopy (TEM) images were taken using a JEM-2100 microscope operating at 200 kV. X-ray photoelectron spectroscopy (XPS) measurements were conducted with a Thermo Scientific ESCALAB 250Xi multifunctional X-ray photoelectron spectroscope under a pressure of 10^{-7} mbar at room temperature.

All rotating disk electrode (RDE) and rotating ring-disk electrode (RRDE) experiments were conducted at room temperature in a three-electrode glass cell, using a Pt wire as a counter electrode, Ag/AgCl (0.210 V *vs.* the SHE, 25 °C) as a reference electrode and a glassy-carbon (GC) electrode as a working electrode.[22] Details about electrode preparation are described in Section S8 in the ESI.† The potential was controlled with an Autolab PGSTAT128N electrochemical workstation. 0.1 M KOH was used as an electrolyte. For each measurement, the electrolyte was first saturated with inert gas by bubbling argon (ultrahigh purity) for 30 min before each experiment and a flow of argon was kept purging over the electrolyte during the measurement. The working electrode was cycled 40 times to obtain a stable surface, with a scan rate of 50 mV s^{-1}. For RDE and RRDE measurements, the electrolyte was pre-saturated

with oxygen (ultrahigh purity) similarly as described above by switching Ar to O_2. The working electrode was scanned cathodically at a rate of 5 mV s^{-1} with varying rotating speeds from 400 rpm to 2025 rpm. Background currents were recorded under Ar at the same scan rate and rotating speed.

Results and discussion

The orthorhombic $SmMn_2O_5$ has a *Pbam* space group, consisting of edge-sharing $Mn^{4+}O_6$ octahedral and $Mn^{3+}O_5$ pyramidal units. Neutron and X-ray diffraction studies demonstrate that the actual symmetry group of mullite family is $Pb2_1m$, allowing for a spontaneous polarization along the *b* axis.[23,24] DFT calculations for bulk $SmMn_2O_5$ were performed on a $(2 \times 1 \times 1)$ unit cell to fit the magnetic period as shown in Fig. 1a according to the reference work.[25–27] The calculated lattice constants of bulk $SmMn_2O_5$ are $a = 7.34$ Å, $b = 8.58$ Å, and $c = 5.66$ Å, which are consistent with previous report.[28] Fig. 1b depicts the total and projected density of states (DOS). The valance band maximum (VBM) is mainly contributed by 3d orbitals of Mn^{3+} and the conduction band minimum (CBM) is mainly contributed by 3d orbitals of Mn^{4+}. Bulk $SmMn_2O_5$ displays antiferromagnetic properties. The magnetic moments of Mn^{3+} and Mn^{4+} are ~3.33 μ_B and ~2.55 μ_B, respectively. A semiconductive character of bulk $SmMn_2O_5$ is observed with a calculated band gap of ~0.34 eV, being less than the experimental value (~1.0 eV) due to the limitation of the GGA description of 3d orbitals.[29–31]

Our previous work has given the schematic phase diagram of the Sm–Mn–O ternary system.[31] The results demonstrate that if we change the Sm-to-Mn ratio, the mullite $SmMn_2O_5$ phase might transform to other lower-order binary oxides, MnO_x, SmO_x, or even Sm or Mn bulk, depending on the chemical potential of each element. In this work, the bulk mullite $SmMn_2O_5$ phase diagram is calculated under ORR conditions by considering not only Sm chemical potential relative to Sm metal ($\Delta\mu_{Sm}$) but also the applied potential *U vs.* the reversible hydrogen electrode (RHE), which is shown in Fig. 2. Calculations were performed for Sm and Mn metals and a series of binary transition metal oxides to determine the phase stability of $SmMn_2O_5$ (see Section S1 in the ESI for calculation details†). A set of oxide precipitation lines are included to constrain the predicted stable region of the bulk $SmMn_2O_5$. These lines represent equilibrium conditions between bulk mullite and lower-order binary metal oxides. At the upper part of the diagram, corresponding to a Sm-rich environment, SmO is the stable phase, where O and Sm coexist in the same amounts. By decreasing the value of $\Delta\mu_{Sm}$ while keeping electrode potential *U* fixed, the most stable phase is Sm_2O_3. The grey shaded area in the plot, which is limited by the Sm_2O_3, Mn_3O_4, Mn_2O_3 and MnO_2 boundary lines, shows that $SmMn_2O_5$ can be stable under ORR conditions. The lower-left corner represents the Sm-poor but Mn-rich environment. From left to right in the lower part of the diagram, the content of Mn in these binary manganese oxides decreases gradually. The vertical grey dashed line represents the limiting potential investigated in this work (*i.e.* 0.8 V *vs.* the RHE). The thermodynamic limiting potential for each catalytic site is determined by the potential-determining step with the smallest reaction Gibbs free energy:

$$U_{\text{limiting}} = \text{Min}_i[-\Delta G_i^0]/ne \quad (1)$$

where *n* is the electron-transfer number for each elementary step (here $n = 1$) and *e* is the elementary charge. The free energy change ΔG_i^0 for each step is defined in eqn (18) in the ESI† with $U = 0$. The lowest overpotential predicted through the theoretical activity plot is 0.43 V (Fig. 6b), at which all ORR steps are either thermoneutral or exergonic. When electrode potential *U*

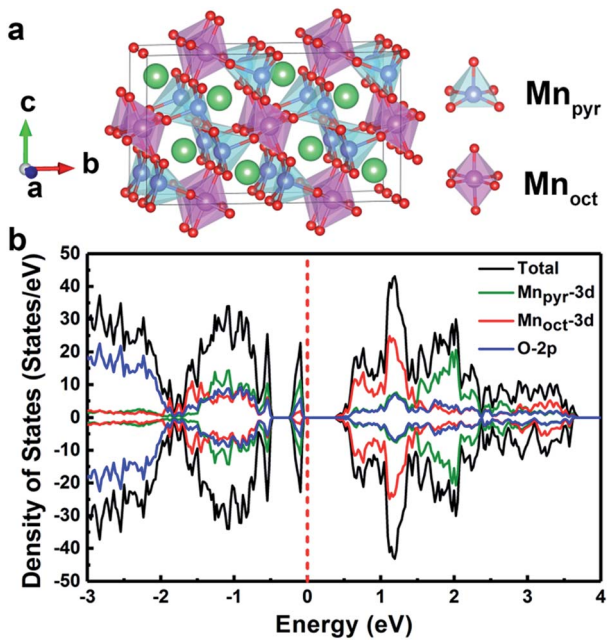

Fig. 1 (a) A $(2 \times 1 \times 1)$ $SmMn_2O_5$ unit cell, the square pyramidal and octahedral ligand fields. The purple, blue, green and red balls represent Mn^{4+}, Mn^{3+}, Sm and O atoms, respectively. (b) The total and projected density of states of bulk $SmMn_2O_5$. The Fermi level is set at zero energy.

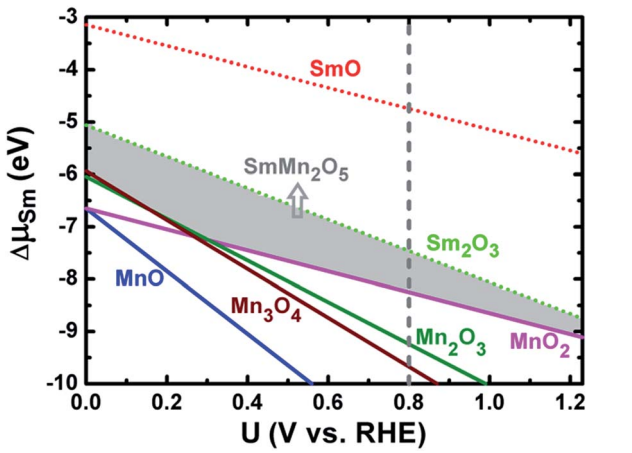

Fig. 2 The bulk $SmMn_2O_5$ mullite phase diagram as a function of Sm chemical potential relative to Sm metal ($\Delta\mu_{Sm}$) and applied potential *U vs.* the RHE.

is above 0.8 V, at least one step in the mechanism would be thermodynamically unfavorable.

Slab models were adopted to simulate $SmMn_2O_5$ surfaces. The size of the supercell is $a = 7.34$ Å, and $b = 8.58$ Å, which is large enough to avoid the long distance interactions between reactants of neighboring supercells.[32] One $p(2 \times 1)$ supercell along the (001) orientation exhibits four distinct terminations, *i.e.* SmO, MnO and two MnO_3 layers, determined by which plane of the four layers is truncated. We should note that these two MnO_3 surfaces are nonequivalent. The MnO_3 terminated surface with the SmO (MnO) surface locating on the sub-layer is labeled as the MnO_3-1 (MnO_3-2) surface. Each slab contains a surface that we concerned and a bottom pseudo-surface (Fig. 3a). Pseudo-surfaces usually have unsaturated atoms with dangling bonds, which introduce spurious in the surface calculations. Sm and O atoms in the bottom layer of the slab are passivated by nitrogen atoms to fill their unsaturated dangling bonds. N atoms are added under bridge sites of every two Sm atoms to form Sm–N bonds with a bond length of 2.53 Å.

The 8-layer (001) MnO_3-2 slab is taken for example (Fig. 3a). We name the atomic layers from bottom to top as layer-1 to layer-8. The comparison of local DOS between MnO_3-2 terminated slabs without and with nitrogen passivation is displayed in Fig. 3c and d. The bottom pseudo-surface has a high density of surface states which might strongly influence top surface chemical reactions as shown in Fig. 3c. Without N passivation, gap states around the Fermi level are not only originated from the surface layer of interest, but also from the bottom pseudo-surface. By adding N atoms under layer-1, the mid-gap states arising from Sm and O dangling bonds are completely suppressed. The behavior of the bottom four layers (layer-1 to layer-4) is similar to that in the bulk $SmMn_2O_5$ with a band gap of ~0.43 eV (see Fig. S1 in the ESI†). This value is slightly larger than that of the bulk, due to the size effect along the *c*-direction. Fig. 3d shows that the gap states decrease gradually from top to bottom layers, indicating the fact that the surface states are mainly caused by the top surface, which means that the bottom pseudo-surface actually acts as an infinite base and leave the top real surface to be precisely studied.

Fig. 4 displays the stability of mullite $SmMn_2O_5$ (001) surfaces at applied potential $U = 0.8$ V *vs.* the RHE as a function of Sm chemical potential relative to the Sm metal, *i.e.* $\Delta\mu_{Sm}$ (see Section S3 in the ESI for calculation details†). Sm chemical potential conditions at which the mullite $SmMn_2O_5$ are in equilibrium with Sm_2O_3 and MnO_2 are indicated by the dashed and solid vertical lines in the plot. The green (pink) shaded area represents the region where binary samarium (manganese) oxides are more stable than mullite $SmMn_2O_5$, while the unshaded area is the stable $SmMn_2O_5$ mullite region. The MnO_3-2 terminated surface has the same stoichiometric ratio as bulk $SmMn_2O_5$ and the stability will not change as Sm chemical potential varies (horizontal line). Meanwhile, MnO_3-1 and MnO_3-2 terminated surfaces are the most stable surfaces we studied within the unshaded area at different Sm chemical potentials.

The electrocatalytic activity of the ORR is governed by the stability of intermediates (O*, OH*, OOH*, and OO*). All the coordinately unsaturated top, bridge and hollow sites of the manganese ions were considered to evaluate their adsorption ability. The adsorption energies of O-containing species were adopted corresponding to those at the most stable adsorption sites. As shown in Fig. 5a, there are two types of hollow sites (H_n and h_n (n = 1, 2, 3, 4)) per $p(2 \times 1)$ (001) MnO surface corresponding to different magnetic arrangements of the

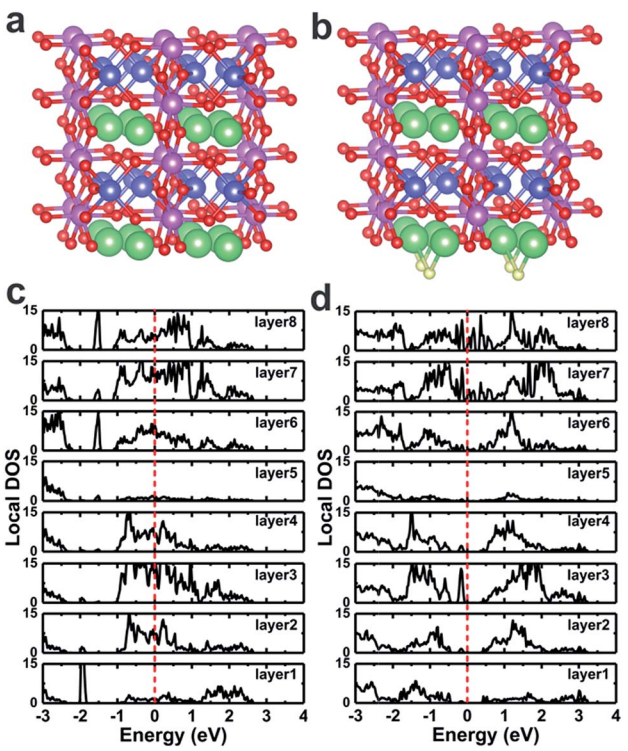

Fig. 3 Side view of the 8-layer (001) MnO_3-2 slabs without (a) and with (b) passivation by N atoms. Local DOS of each atomic layer for MnO_3-2 slabs without (c) and with (d) passivation by N atoms. The purple and blue balls represent Mn ions; green, red and yellow balls represent Sm, O and N atoms, respectively.

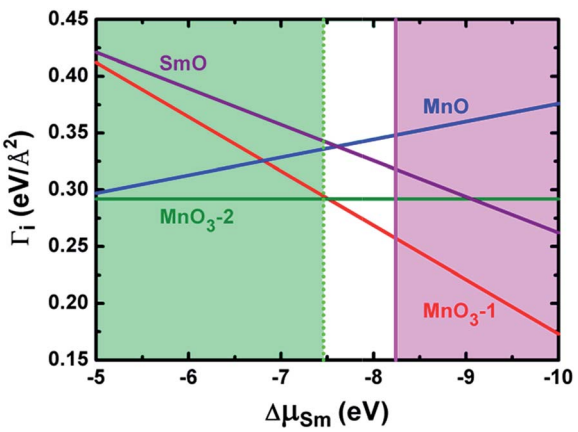

Fig. 4 The stability of mullite $SmMn_2O_5$ (001) surfaces at an applied potential of 0.8 V *vs.* the RHE as a function of $\Delta\mu_{Sm}$. The MnO_3-1, MnO_3-2, MnO, and SmO surfaces are represented by red, green, blue, and purple solid lines, respectively.

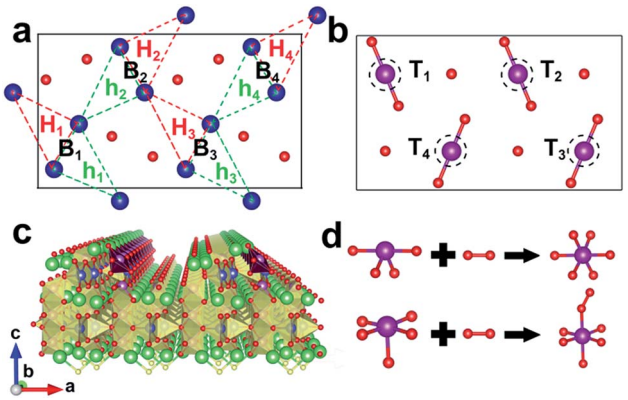

Fig. 5 Top view of (001) (a) MnO surface layer and (b) MnO_3 surface layer. (c) A specific stepped surface. (d) Schematic of the adsorption configurations of the oxygen molecules. The purple and blue balls represent Mn atoms, the green, red and yellow balls represent Sm, O and N atoms, respectively.

surrounding Mn atoms. The bridge sites B_n (n = 1, 2, 3, and 4) locate on the top of Mn–Mn dimers with a dimer length of 3.11 Å. All oxygen atoms of the surface have the same local environment. For the bare MnO surface, the most stable adsorption position for one O* atom is the H_n site, so as to OOH* and OO*. But for OH*, the most stable location is the B_n site. To investigate the influence of oxygen coverage on the adsorption ability, the adsorptions of two to four O atoms are considered. For MnO + 2O*, the most stable adsorption configuration is h_1 + h_4. For MnO + 3O*, one oxygen atom prefers the h_1 site and the other two O* prefer b_3 and b_4 sites. b_1 to b_4 sites are all occupied by O* atoms for MnO + 4O*. The less oxidized MnO surface exhibits strong oxygen coverage dependence, giving large difference in binding energies. The bonding strengths between adsorbates and surface active sites become weaker as the oxygen coverage increases. The top view of the MnO_3 surface (MnO_3-1 or MnO_3-2 surface) is displayed in Fig. 5b. The nearest distance of every two Mn ions in this surface is 5.64 Å with one O atom between them. Intermediates can only be adsorbed on the top of Mn ions (T_n, (n = 1, 2, 3, and 4)). The geometry of reconstructed surface sites such as steps, kinks or terraces plays an important role in the catalytic reaction. A specific stepped surface was constructed as shown in Fig. 5c. The Mn ions in the irregular purple square pyramids are the reaction sites. The adsorptions of the ORR intermediates tend to compensate the coordination of manganese atoms to form Mn-centered octahedral or pyramidal crystal fields, as shown in Fig. 5d. This principle can also be applied to other adsorption sites. According to d-band theory, the molecular adsorption ability of active sites of the transition metal catalyst is closely related to the d-band center position relative to the Fermi level. The higher the d-band center, the higher the adsorption energy.[14] The d-band centers of Mn atoms in MnO, MnO_3-1 and MnO_3-2 surfaces are −1.26 eV, −2.21 eV, and −1.48 eV, respectively, indicating a stronger molecular adsorption ability of the MnO surface.

Scaling relationships between the adsorption energies of reaction intermediates are generalized in Fig. 6a (calculation details can be found in Section S4 in the ESI†). A range of more

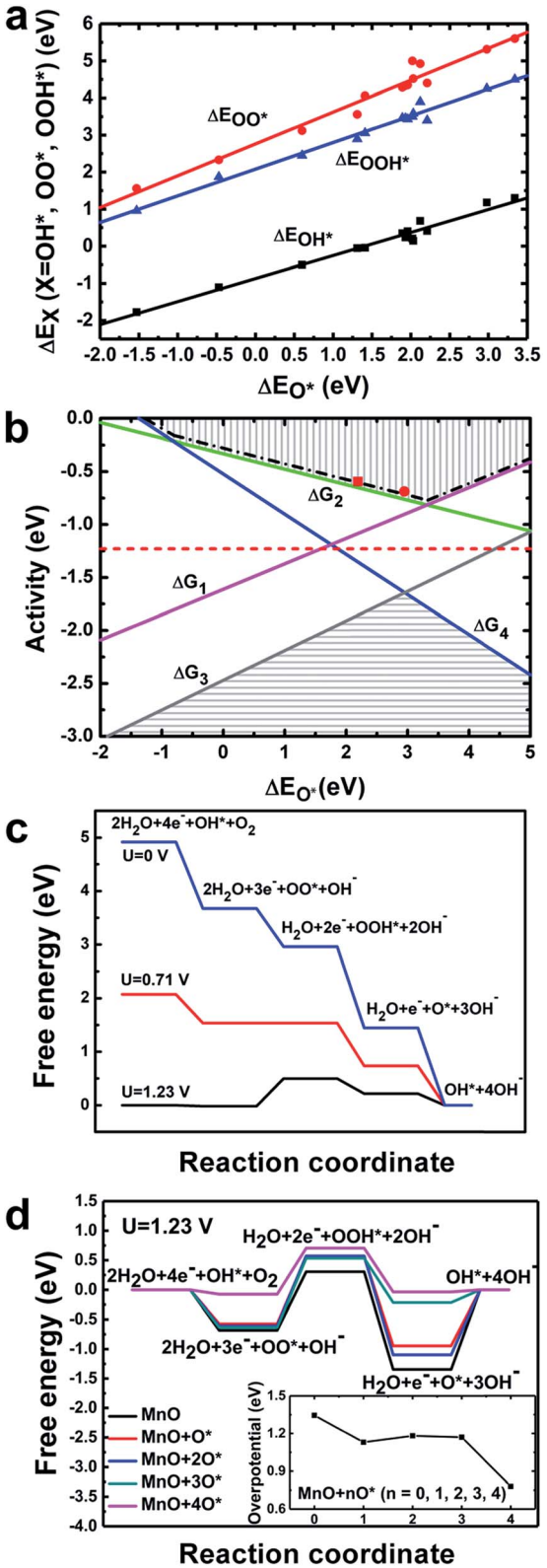

Fig. 6 (a) The linear relationship of binding energies of OH* (black squares), OOH* (blue triangles) and OO* (red circles) *versus* O*. The fits to the data points are $\Delta E_{OH*} = 0.62\Delta E_{O*} - 0.87$ eV, $\Delta E_{OOH*} = 0.72\Delta E_{O*} + 2.08$ eV and $\Delta E_{OO*} = 0.86\Delta E_{O*} + 2.68$ eV, respectively. (b) The theoretical activity of the ORR as a function of the oxygen binding energy. (c) Free energy diagram of the oxygen reduction reaction over the stepped surface at different potentials. (d) The free energy diagram under different oxygen coverages at the equilibrium potential U = 1.23 V. The insert is the trend of the overpotential while changing the oxygen coverage over the MnO surface.

than five electron volts for O* binding energies (ΔE_{O*}) is found by examining various adsorption sites on diverse surfaces at different oxidized and reduced levels. The slope among the linear fits of all facets is 0.62 for the adsorption energies of OH* *versus* O*, 0.72 for OOH* *versus* O*, and 0.86 for OO* *versus* O*, while the corresponding offsets are −0.87 eV, 2.08 eV and 2.68 eV, respectively. This means that $SmMn_2O_5$ surfaces that bind O* strongly also bind OH*, OOH*, and OO* strongly. Trends of the slopes fulfill the octet rule.[33] For instance, the slope (~0.62) of the linear relationship for ΔE_{OH*} *versus* ΔE_{O*} is approximately the same as the one (~0.5) found for metal surfaces. With the above linear relationship among the binding energies of the intermediates, it is important to construct the volcano plot as a function of only one parameter (ΔE_{O*}) to identify the active sites. The calculation details are shown in Section S5 in the ESI.†

We consider the following four-electron reaction paths in eqn (1)–(4):

$$OH^* + O_2 + e^- \rightarrow OO^* + OH^- \quad (2)$$

$$OO^* + H_2O + e^- \rightarrow OOH^* + OH^- \quad (3)$$

$$OOH^* + e^- \rightarrow O^* + OH^- \quad (4)$$

$$O^* + H_2O + e^- \rightarrow OH^* + OH^- \quad (5)$$

The theoretical activity of the four-electron transfer steps is shown in Fig. 6b. The *y*-axis is the activity defined as the change of the free energy (ΔG) of the different reaction steps. For strong and weak O* binding on the oxide surfaces, the ORR activity is limited by the OOH* formation (green line) and the displacement of OH* by the resulting volcano is indicated by dash-dotted lines and the hatched area. Overpotentials of 0.52 V and 0.54 V are identified over the specific stepped surface (the red circle) and the MnO_3-1 surface (the red square), respectively. The volcano plot shows that reaction sites with an O* binding energy around 3.4 eV should have a higher rate of oxygen reduction. The corresponding overpotential is 0.43 V, even the specific active site is not accessible yet. Further work is still required to optimize the surface *via* introducing defects, interfaces, morphology control *etc.* The free energy diagram of the stepped surface is presented in Fig. 6c at zero cell potential, at the highest potential where all the reaction steps are downhill in free energy, and at the equilibrium potential. At the equilibrium potential $U = 1.23$ V, the hydrogenation from OO* to OOH* is endothermic, with an energy difference of $\Delta G_2 = 0.52$ eV, which gives an output cell bias of 0.71 V. The free energy diagram corresponding to the MnO_3-1 surface is almost the same as Fig. 6c with the difference in $\Delta G_2 = 0.54$ eV. Fig. 6d shows the calculated free energy diagram of the MnO surface with different oxygen coverages. We conclude that the MnO surface with low oxygen coverage binds too strong with oxygen. Thus the adsorbed OO*, O* and OH* cannot be easily removed from the surface, in other words, the surface is oxidized.[34] The overpotential decreases as the oxygen coverage increases with slight fluctuation. This is because the ORR species are coupled strongly to surface coverage, as well as the local oxidation states. The overpotential, which is directly linked with the ORR efficiency, reaches 0.78 V, when all these four dimers are occupied by O atoms on the bridge sites, *i.e.* the MnO + 4O* surface.

Based on the above understanding, we synthesized relevant catalysts to validate the theoretical predictions. A hydrothermal method was adopted for the preparation of mullite $SmMn_2O_5$. A reference sample was synthesized *via* a similar procedure without adding samarium nitrate. In Fig. 7a(ii), all the diffraction peaks match well with those for the standard $SmMn_2O_5$ (ICDD PDF# 52-1096), indicating that pure-phase mullite was successfully synthesized. In the absence of samarium, however, a mixture of manganese oxides (MnO_x) was obtained. Based on the XRD spectrum in Fig. 7a(i), at least two phases, γ-MnOOH (ICDD PDF# 18-0805) and α-MnO_2 (ICDD PDF# 44-0141) could probably be recognized. The broadened peaks and low signal-to-noise ratio imply the poor degree of crystallinity. The morphology of MnO_x was revealed by TEM in Fig. 7c. The absence of samarium nitrate would yield aggregated nanoparticles and partial nanorods. From the low-magnification SEM image in Fig. 7b, it can be visualized that the panoramic morphology of the prepared $SmMn_2O_5$ powder consists of a uniform 1-D structure. The TEM images in Fig. S8† reveal that mullite nanorods (NRs) develop to form the bundle-like morphology, which are actually composed of a few primary nanowires aggregated along the axial direction. From the high-resolution TEM image presented in Fig. 7d, the diameter of a single $SmMn_2O_5$ nanowire is examined to be ~6 nm. Clear lattice fringes are observed and the lattice spacing is 0.571 nm, corresponding to the interplanar distance of the (001) plane. This fact indicates that the nanowire-structured $SmMn_2O_5$ was well-crystallized and tended to grow along the [001] direction.

XPS was adopted to further reveal the surface composition of the as-prepared samples and the chemical states of samarium

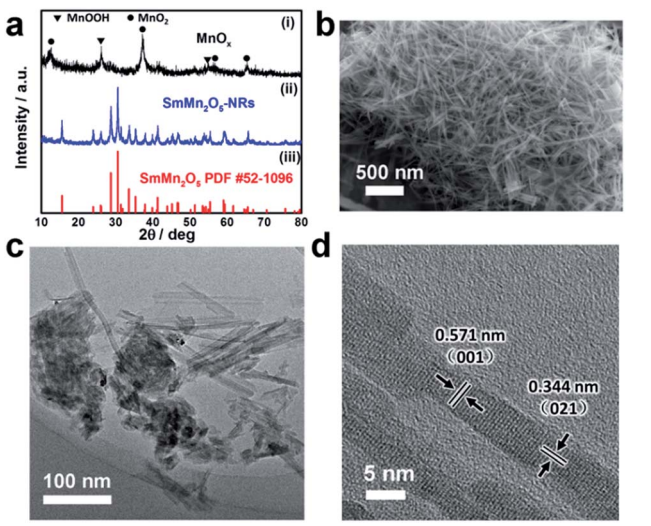

Fig. 7 (a) XRD spectra of the as-prepared samples and the reference spectrum of $SmMn_2O_5$. (b) SEM image of mullite nanorods. (c) A representative TEM image of the MnO_x mixture. (d) HRTEM image of mullite nanorods.

(Sm) and manganese (Mn). Fig. 8a shows the full spectrum of $SmMn_2O_5$-NRs. The signals of Sm, Mn, O and C were detected, while all other impurity elements were under the detection limit. All binding energies (BEs) were calibrated by using C 1s BE of 284.9 eV. The Sm 3d spectra of $SmMn_2O_5$-NRs and MnO_x are presented in Fig. 8b, and the data of pure Sm_2O_3 were also recorded for reference. Sm_2O_3 (99.9%) was bought from Aladdin® and used as received without further purification. The corresponding XRD spectrum is provided in Fig. S7.† Note that the shape and peak positions of the Sm spectrum of $SmMn_2O_5$-NRs are nearly identical to those of Sm_2O_3, which is strong evidence that the above two materials share a similar valance of Sm near the surface. The Sm $3d_{3/2}$ and $3d_{5/2}$ peaks are observed at 1110.1–1110.2 eV and 1083.0–1083.2 eV, respectively, demonstrating that Sm exists as Sm^{3+} in the near surface region.[35] In contrast, no obvious Sm signal was detected in the MnO_x sample. In Fig. 8c, the Mn $2p_{1/2}$ and $2p_{3/2}$ peaks of $SmMn_2O_5$-NRs are obtained at 652.9 eV and 641.4 eV with a spin orbit splitting of 11.5 eV. These observations are very similar to those in the previous literature.[31] The Mn $2p_{3/2}$ component could be fitted by two sub-peaks at 641.1 eV and 642.2 eV referring to the contribution of Mn^{3+} and Mn^{4+}, respectively.[36–38] The fitted profile conforms well to the background-subtracted Mn 2p profile. The atomic ratio between Mn^{3+} and Mn^{4+} is calculated to be 1 : 0.97, implying that the average valance state of Mn near the surface of $SmMn_2O_5$-NRs is very close to 3.5. This phenomenon agrees with the results obtained from $SmMn_2O_5$ nanoparticles prepared *via* a co-precipitation method and the reference work on $DyMn_2O_5$.[16,39] For the Mn $2p_{3/2}$ profile of MnO_x, however, at least three chemical states could be recognized, alluding more complex surfaces.

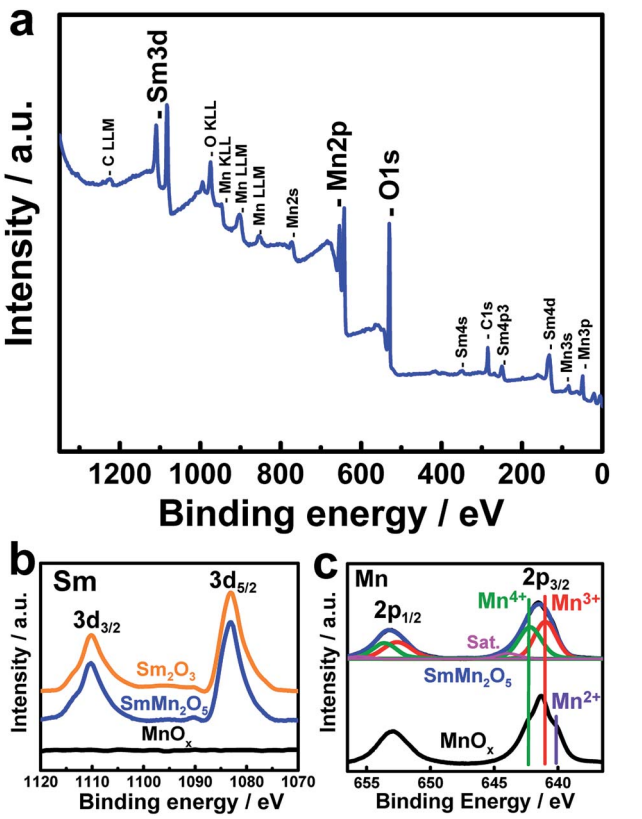

Fig. 8 (a) Full XPS spectrum of $SmMn_2O_5$-NRs. (b) Sm 3d spectra of Sm_2O_3 and $SmMn_2O_5$. (c) Mn 2p spectra of $SmMn_2O_5OO^*$ (pink line), respectively.

The as-prepared catalysts were deposited on GC electrodes for electrochemical reduction of oxygen. All of the thin-film electrodes had a composition of 250 μg_{oxide} cm_{disk}^{-2} and/or 150 μg_{carbon} cm_{disk}^{-2} unless they are stated to be different. For Pt/C, 25 μg_{Pt} cm_{disk}^{-2} was applied to the working electrode without adding any extra carbon. Fig. 9a shows the linear sweep voltammetry (LSV) curves of $SmMn_2O_5$-NRs mixed with carbon powder ($SmMn_2O_5$-NRs/C) and commercial Pt/C at a rotating speed of 1600 rpm and a scan rate of 5 mV s^{-1}. Data for pure $SmMn_2O_5$-NRs, pure carbon and MnO_x mixed with carbon (MnO_x/C) were also recorded for comparison. All the potentials in the experimental part were referenced to the RHE scale after background correction and *iR*-compensation.[40,41] The uncompensated electrolyte resistance R_S (~42 Ω) between working and reference electrodes was measured through high frequency alternating-current (AC) impedance (see Section S10 in the ESI†). The oxygen reduction activity can be estimated visually from onset potential, which is here defined as the potential corresponding to 5% of diffusion-limited current density. The poor current–potential response of carbon implies that it merely contributes slightly to the ORR activity. Through a simple physical mixing of $SmMn_2O_5$-NRs and carbon, the $SmMn_2O_5$-NRs/C catalyst obviously shows much enhanced catalytic activity. The diffusion-limited current density of $SmMn_2O_5$-NRs increases from 1.47 mA cm^{-2} to 5.45 mA cm^{-2} after being mixed with carbon. Electrical conductivity should be a key factor in affecting the catalytic activities of metal oxides.[42] The onset potential of $SmMn_2O_5$-NRs/C is 0.817 V, while it is 0.756 V for MnO_x/C. The $SmMn_2O_5$-NRs/C also shows a larger diffusion-limited current density of 5.45 mA cm^{-2} compared to the Sm-free sample MnO_x/C. In Fig. 9b, the Tafel slopes of Pt/C and $SmMn_2O_5$-NRs/C are both close to 60 mV dec^{-1}, which corresponds to $2.3RT/F$ at room temperature for platinum-based catalysts.[43] It is worth noting that $SmMn_2O_5$-NRs/C displays a much smaller Tafel slope than pure $SmMn_2O_5$-NRs (close to 120 mV dec^{-1}), which is another piece of evidence of enhanced ORR kinetics.

The number of electron transferred *n* on $SmMn_2O_5$-NRs/C and Pt/C catalysts can be extracted from the Koutecky–Levich (K–L) analysis conducted from LSV curves at various rotating speeds from 400 to 2025 rpm (Fig. S4†). Fig. S4c† shows that in alkaline media, the commercial Pt/C catalyst reduces oxygen to OH^- *via* a direct four-electron pathway. The calculated *n* values of $SmMn_2O_5$-NRs/C (Fig. S4d†) are also close to four in the range of 0.40 V to 0.60 V *vs.* the RHE, which is highly consistent with the RRDE analysis shown in Fig. S5b† and 9c. For $SmMn_2O_5$-NRs/C, the HO_2^- proportion slightly increases when the disk potential decreases. Probably, this observation could be partially attributed to the oxygen reduction *via* the two-electron pathway or indirect four-electron pathway, both of which will lead to the production of hydrogen peroxide. Our DFT calculations provided evidence for the existence of the two-electron

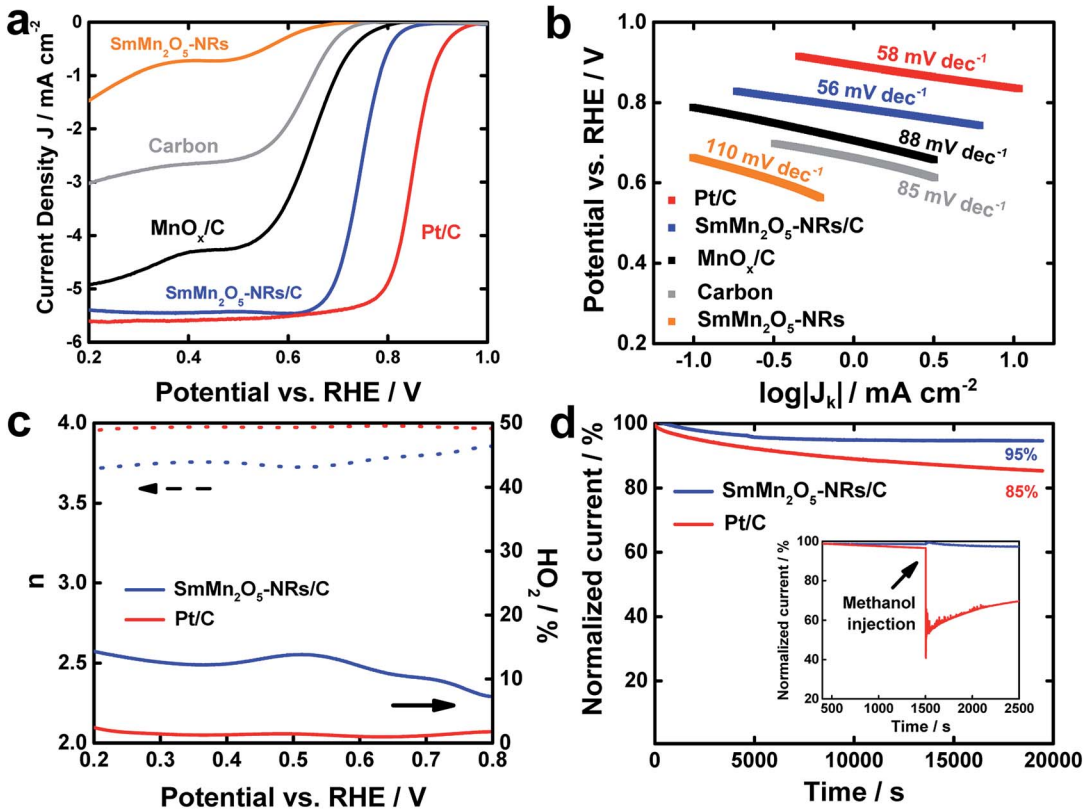

Fig. 9 (a) LSV curves of oxygen reduction on pure $SmMn_2O_5$, carbon, MnO_x/C, $SmMn_2O_5$-NRs/C and Pt/C in O_2-saturated 0.1 M KOH at a rotating speed of 1600 rpm with a scan rate of 5 mV s^{-1} and (b) the corresponding Tafel plots. (c) Number of electron transferred n and HO_2^- yield of $SmMn_2O_5$-NRs/C and Pt/C extracted from RRDE measurements. (d) Chronoamperometric curves of $SmMn_2O_5$-NRs/C and Pt/C at a constant potential of 0.6 V *vs.* the RHE. The inset shows the effect of methanol injection.

pathway on $SmMn_2O_5$ surfaces. The limiting potential of the four-electron pathway (*i.e.* 0.8 V) is much higher than that of the two-electron (*i.e.* 0.24 V), which makes the four-electron pathway dominant for ORR processes. More details can be found in Section S6 in the ESI.†

We further evaluated the stability of $SmMn_2O_5$-NRs/C and Pt/C *via* chronoamperometric measurement in O_2-saturated 0.1 M KOH (Fig. 9d). The applied potential was maintained at 0.60 V *vs.* the RHE. Before measurement, the working electrode was cycled 30 times to obtain a stable surface. The $SmMn_2O_5$-NRs/C electrode shows a current decrease at the first 10 000 s and then reaches a constant. After 20 000 s, the activity still remains ~95%. For Pt/C electrode, however, the current keeps dropping during the test, leaving only ~85% of the original performance after 20 000 s. This fact implies that the mullite catalyst unequivocally shows higher stability than Pt/C. Fig. 9d inset provides the effect of methanol injection. No obvious current fluctuation is observed on the $SmMn_2O_5$-NRs/C electrode after the introduction of methanol, suggesting excellent methanol tolerance of mullite catalysts and the potential application in direct methanol fuel cells (DMFCs). By contrast, the commercial Pt/C catalyst is found to be very sensitive to methanol.

Although the RRDE is the best known method to evaluate the production of hydrogen peroxide, there has been limited research on the influence of the catalyst loading on the yield of hydrogen peroxide. Previous literature found that the percentage of H_2O_2 released into the electrolyte had a strong loading dependence for the Fe–N–C electrocatalyst.[44] One reasonable explanation is that the film electrode tends to form a porous 3-D structure rather than a planar substrate under high catalyst loading, and the saturated-current density could possibly increase considering the fact that the H_2O_2 produced far from the electrode/electrolyte interface (or near the GC electrode inside the active layer) may be further reduced before being detected by the ring electrode. To further investigate the oxygen reduction pathway on the surface of mullite $SmMn_2O_5$, oxide loadings varying from 25 to 250 μg cm_{disk}^{-2} were applied to the GC electrode. Typically, a uniform dark film over the entire surface of the GC electrode could be obtained. As shown in Fig. 10a, a limited-current plateau is obtained for each loading, while the value decreases from 5.45 mA cm^{-2} to 3.66 mA cm^{-2} with decreasing loading. The ring currents were divided by collection efficiency N_c, making them more comparable to the disk currents. At medium and high loadings (50–250 μg_{oxide} cm_{disk}^{-2}), the ring current density increases while the loading is reduced, which is evidence of the increase of HO_2^- fraction being detected. At extremely low loading (25 μg cm_{disk}^{-2}), the ring current starts to become lower, which could be attributed to the decrease of active site number. The corresponding n is summarized in Fig. 10b. Generally, n decreases as the loading decreases while little variation of n was observed

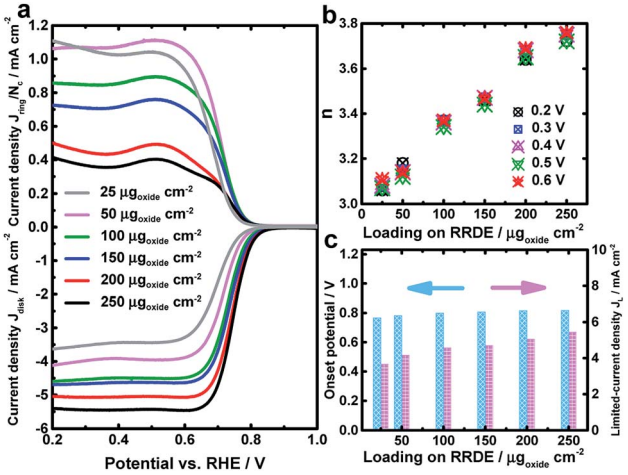

Fig. 10 (a) Oxygen reduction current densities on the disk and the corresponding ring current densities for various loadings of catalyst. The ring current densities were divided by collection efficiency N_c. (b) The number of electron transferred (n) at different loadings and potentials. (c) Dependence of onset potential and limited-current density onto different loadings.

over different potentials. It is noticeable that for loading as low as 25 μg cm$_{disk}^{-2}$, n is still around 3.1, demonstrating that the four-electron pathway remains dominant for oxygen reduction on the surfaces of $SmMn_2O_5$-NRs. Since the limited-current density increases with the loadings (Fig. 10c), and this part of current augment is contributed by the further electrochemical reduction of HO_2^- as discussed above, it could be concluded that the reduction of this fraction of HO_2^- is primarily the faradic process. Most of HO_2^- is electrochemically reduced to OH^- rather than self-destructed into of OH^- and O_2.[45] The ORR which occurs on the surfaces of $SmMn_2O_5$-NRs mainly follows a direct four-electron pathway, while partially going through an indirect four-electron pathway.[46]

It should be noted that the ORR activity of the $SmMn_2O_5$ catalyst is comparable to the state-of-art binary manganese oxides in terms of a combined evaluation of onset potential (0.817 V), half-wave potential (0.746 V), electron transfer number (3.78) (Table S1†) and stability.[47,48] Even though more efforts are indispensable for a better understanding of the ORR mechanism on surfaces of Mn-mullite, our investigation still provides an insight into the future design of metal-oxide-based electrocatalysts. On one hand, the performance of mullite catalysts can be improved by exposing more active sites through precise morphology control or exploring novel synthesis methods to reduce particle size. On the other hand, considering the fact that surface oxygen coverage has a significant impact on the overpotential, the ORR activity of mullite catalysts can also be optimized by facilitating oxygen adsorption and diffusion, such as coupling oxygen storage materials (CeO_2) or tuning oxygen defects.

Conclusions

We have demonstrated that $SmMn_2O_5$ is a promising electrocatalyst for the oxygen reduction reaction by combining theoretical calculations and experimental validations. DFT modelling was introduced to investigate possible reaction mechanisms. To obtain a well-defined slab model, the mid-gap states arising from the pseudo-surface were eliminated by nitrogen passivation. We found that ΔE_{O*}, as a descriptor, could be used to search the geometric structure of surface sites which are catalytically active. $SmMn_2O_5$ is predicted to catalyze four-electron reduction of O_2 at low overpotential (0.43 eV). To verify the theoretical prediction, $SmMn_2O_5$-NRs were prepared through a hydrothermal method. We have shown that the $SmMn_2O_5$-NRs/C presents favorable catalytic activity and superior stability to commercial Pt/C. An overpotential as low as 0.413 V was observed, which is comparable to the activity of most binary manganese oxides, while enabling a higher limiting current. Based on K–L and RRDE analysis, the number of electrons transferred on the surface of the mullite catalyst was close to four, which is in good agreement with our calculation. According to the structure–function relationship, this would provide a strategy towards the rational design of non-precious ORR electrocatalyst materials through precise morphology control or tuning of the A-site element.

Conflicts of interest

There are no conflicts to declare.

Acknowledgements

This work is supported by the National Key Research and Development Program (Grant No. 2016YFB0901600), the National Natural Science Foundation of China (21573117 and 11404172), the 1000 Youth Talents Plan, Tianjin Natural Science Foundation (14JCZDJC37700), and the National Basic Research Program of China (973 Program with No. 2014CB931703).

References

1 P. M. Woodward, H. Mizoguchi, Y. I. Kim and M. W. Stoltzfus, *In Metal Oxides: Chemistry and Applications*, ed. J. L. G. Fierro, Chemical Rubber Company, Boca Raton, 2006, Vol. 6, p. 140.
2 K. L. Pickrahn, S. W. Park, Y. Gorlin, H.-B.-R. Lee, T. F. Jaramillo and S. F. Bent, *Adv. Energy Mater.*, 2012, **2**, 1269–1277.
3 Y. Tan, C. Xu, G. Chen, X. Fang, N. Zheng and Q. Xie, *Adv. Funct. Mater.*, 2012, **22**, 4584–4591.
4 M. Fayette, A. Nelson and R. D. Robinson, *J. Mater. Chem. A*, 2015, **3**, 4274–4283.
5 Y. Wu, Q. Shi, Y. Li, Z. Lai, H. Yu, H. Wang and F. Peng, *J. Mater. Chem. A*, 2015, **3**, 1142–1151.
6 Y. J. Sa, K. Kwon, J. Y. Cheon, F. Kleitz and S. H. Joo, *J. Mater. Chem. A*, 2013, **1**, 9992–10001.
7 D. Chen, C. Chen, Z. M. Baiyee, Z. Shao and F. Ciucci, *Chem. Rev.*, 2015, **115**, 9869–9921.
8 J. Suntivich, H. A. Gasteiger, N. Yabuuchi, H. Nakanishi, J. B. Goodenough and Y. Shao-Horn, *Nat. Chem.*, 2011, **3**, 546–550.

9 B. Hammer, *Top. Catal.*, 2006, **37**, 3–16.
10 M. Yung, E. Holmgreen and U. Ozkan, *J. Catal.*, 2007, **247**, 356–367.
11 M. Kang, E. D. Park, J. M. Kim and J. E. Yie, *Appl. Catal., A*, 2007, **327**, 261–269.
12 C. H. Kim, G. Qi, K. Dahlberg and W. Li, *Science*, 2010, **327**, 1624–1627.
13 W. T. Hong, M. Risch, K. A. Stoerzinger, A. Grimaud, J. Suntivich and Y. Shao-Horn, *Energy Environ. Sci.*, 2015, **8**, 1404–1427.
14 B. Hammer and J. K. Nørskov, *Adv. Catal.*, 2000, **45**, 71–129.
15 W. Wang, G. McCool, N. Kapur, G. Yuan, B. Shan, M. Nguyen, U. M. Graham, B. H. Davis, G. Jacobs, K. Cho and X. Hao, *Science*, 2012, **337**, 832–835.
16 Y. Li, X. Zhang, H.-B. Li, H. D. Yoo, X. Chi, Q. An, J. Liu, M. Yu, W. Wang and Y. Yao, *Nano Energy*, 2016, **27**, 8–16.
17 G. Kresse and J. Furthmiiller, *Comput. Mater. Sci.*, 1996, **6**, 15–50.
18 G. Kresse and J. Hafner, *Phys. Rev. B*, 1993, **47**, 558–561.
19 G. Kresse and J. Furthmüller, *Phys. Rev. B*, 1996, **54**, 11169–11186.
20 P. E. Blöchl, *Phys. Rev. B*, 1994, **50**, 17953–17979.
21 G. Zhu, P. Liu, M. Hojamberdiev, B. Ge, Y. Liu, H. Miao and G. Tan, *Mater. Chem. Phys.*, 2009, **118**, 467–472.
22 Y. Garsany, O. A. Baturina, K. E. Swider-Lyons and S. S. Kocha, *Anal. Chem.*, 2010, **82**, 6321–6328.
23 J. A. Alonso, M. T. Casais, M. J. Martinez-Lope, J. L. Martinez and M. T. Fernandez-Diaz, *J. Phys.: Condens. Matter*, 1997, **9**, 8515–8526.
24 L. C. Chapon, G. R. Blake, M. J. Gutmann, S. Park, N. Hur, P. G. Radaelli and S. W. Cheong, *Phys. Rev. Lett.*, 2004, **93**, 177402.
25 T.-R. Chang, H.-T. Jeng, C.-Y. Ren and C.-S. Hsue, *Phys. Rev. B*, 2011, **84**, 024421.
26 C. Wang, G. C. Guo and L. He, *Phys. Rev. Lett.*, 2007, **99**, 177202.
27 G. Giovannetti and J. van den Brink, *Phys. Rev. Lett.*, 2008, **100**, 227603.
28 I. Kagomiya, K. Kohn and T. Uchiyama, *Ferroelectrics*, 2002, **280**, 131–143.
29 L. J. Sham and M. Schlüter, *Phys. Rev. Lett.*, 1983, **51**, 1888–1891.
30 J. P. Perdew and M. Levy, *Phys. Rev. Lett.*, 1983, **51**, 1884–1887.
31 H.-B. Li, Z. Yang, J. Liu, X. Yao, K. Xiong, H. Liu, W.-H. Wang, F. Lu and W. Wang, *Appl. Phys. Lett.*, 2016, **109**, 211903.
32 K. Berland, V. R. Cooper, K. Lee, E. Schroder, T. Thonhauser, P. Hyldgaard and B. I. Lundqvist, *Rep. Prog. Phys.*, 2015, **78**, 066501.
33 F. Calle-Vallejo, D. Loffreda, M. T. Koper and P. Sautet, *Nat. Chem.*, 2015, **7**, 403–410.
34 V. Stamenkovic, B. S. Mun, K. J. Mayrhofer, P. N. Ross, N. M. Markovic, J. Rossmeisl, J. Greeley and J. K. Norskov, *Angew. Chem., Int. Ed.*, 2006, **45**, 2897–2901.
35 Y. Ding, X. Zhang, H. Zhu and J.-J. Zhu, *J. Mater. Chem. C*, 2014, **2**, 946–952.
36 A. Machocki, T. Ioannides, B. Stasinska, W. Gac, G. Avgouropoulos, D. Delimaris, W. Grzegorczyk and S. Pasieczna, *J. Catal.*, 2004, **227**, 282–296.
37 D. Delimaris and T. Ioannides, *Appl. Catal., B*, 2008, **84**, 303–312.
38 Y. Zhang-Steenwinkel, J. Beckers and A. Bliek, *Appl. Catal., A*, 2002, **235**, 79–92.
39 Z. Y. Zhao, M. F. Liu, X. Li, J. X. Wang, Z. B. Yan, K. F. Wang and J. M. Liu, *J. Appl. Phys.*, 2014, **116**, 054104.
40 K. Shinozaki, J. W. Zack, R. M. Richards, B. S. Pivovar and S. S. Kocha, *J. Electrochem. Soc.*, 2015, **162**, F1144–F1158.
41 J. Suntivich, H. A. Gasteiger, N. Yabuuchi and Y. Shao-Horn, *J. Electrochem. Soc.*, 2010, **157**, B1263.
42 F. Cheng, Y. Su, J. Liang, Z. Tao and J. Chen, *Chem. Mater.*, 2010, **22**, 898–905.
43 U. A. Paulus, T. J. Schmidt, H. A. Gasteiger and R. J. Behm, *J. Electroanal. Chem.*, 2001, **495**, 134–145.
44 A. Bonakdarpour, M. Lefevre, R. Yang, F. Jaouen, T. Dahn, J.-P. Dodelet and J. R. Dahn, *Electrochem. Solid-State Lett.*, 2008, **11**, B105.
45 Z. W. Seh, J. Kibsgaard, C. F. Dickens, I. Chorkendorff, J. K. Norskov and T. F. Jaramillo, *Science*, 2017, **355**, 6321.
46 W. Xiao, D. Wang and X. W. Lou, *J. Phys. Chem. C*, 2010, **114**, 1694–1700.
47 Y. Gorlin and T. F. Jaramillo, *J. Am. Chem. Soc.*, 2010, **132**, 13612–13614.
48 K. A. Stoerzinger, M. Risch, B. Han and Y. Shao-Horn, *ACS Catal.*, 2015, **5**, 6021–6031.